
Designing Optimal Transport Flows

Shimon Malnick¹ Matan Rusanovsky¹ Ohad Fried² Shai Avidan¹

¹Tel Aviv University ²Reichman University

{malnick,matanru}@mail.tau.ac.il ofried@runi.ac.il avidan@eng.tau.ac.il

Project page: malnick.net/designing_ot_flows

Abstract

Flow matching models learn to transport samples from a simple prior distribution to a complex data distribution. When prior-data pairs are coupled via optimal transport (OT), the learned trajectories are straight and non-crossing, enabling fast, even single-step, generation. However, computing the OT coupling in high dimensions is intractable, and existing methods attempt to solve the OT problem, at the cost of persistent bias or significant overhead. Rather than solving for the OT coupling, we reformulate the problem. Once the prior is treated as a design choice rather than a fixed input, the OT coupling between prior and data is no longer unique. Many priors admit an OT-optimal identity coupling to the data, leaving us free to choose one that is also tractable to sample. We identify low-frequency projection of natural images as such a choice. The identity coupling between data and its low-frequency representation is empirically OT-optimal, the prior is structured enough to be sampled by a lightweight model at inference, and the remaining flow-matching task reduces to synthesizing high-frequency detail. Interpolating the prior with Gaussian noise further improves generation quality while preserving the OT coupling. The approach requires no modifications to the flow model itself, and integrates naturally with latent-space models, classifier-free guidance, and one-step generation frameworks. Across all benchmarks, our method reduces trajectory curvature by more than $2\times$ compared to existing flow matching methods, yielding better generation quality in the few-step regime.

1 Introduction

Generative models have become one of the most transformative tools in modern machine learning. In just a few years, they have scaled to produce photorealistic images at high resolution [10, 31, 38, 44], generate temporally coherent video [23, 14, 42, 18], and are rapidly expanding to new modalities including audio [33, 39, 4], 3D [21, 32], and beyond [24, 51]. They are the backbone of both open-source and commercial generation systems [10, 31, 42], powering creative tools used by millions.

At the heart of every generative model lies a single conceptual task, learn to transform a simple, easy-to-sample distribution into a complex, unknown target distribution from which we only observe finite samples. If one could compute the optimal transport (OT) map between a simple distribution and the true underlying data distribution, generation would reduce to a single map evaluation, transforming any noise sample directly into a data sample. This would be the perfect generator, a direct and cost-minimizing transformation from noise to data, and the ideal we aim to approach, high-quality generation in as few steps as possible, ideally just one.

But this map is out of reach. Computing the optimal transport coupling between a high-dimensional data distribution and a standard Gaussian prior is computationally prohibitive at modern scales. Exact solvers scale cubically in the number of samples [30], while entropic relaxations [7] remain prohibitive in the dimensionalities of modern data. Faced with this intractability, the field turned to flow matching [36, 37, 1]. Rather than computing the transport map directly, flow matching learns a

velocity field that continuously deforms the simple distribution into the data distribution over a unit time interval. In standard practice, this velocity field is trained on independently sampled noise-data pairs, forgoing any global coupling structure. This has proven remarkably effective, and flow-based architectures now underpin the leading generation systems [10, 31, 14, 23].

Yet flow matching inherits a fundamental tension from the intractability it circumvents. Since the true OT coupling is unknown, standard training pairs noise and data independently at random. This forces the learned velocity field to average over conflicting transport directions, producing curved, crossing trajectories that demand many integration steps at inference [43, 52]. This is the central obstacle to efficient few-step and single-step generation, since straighter trajectories require fewer steps to traverse.

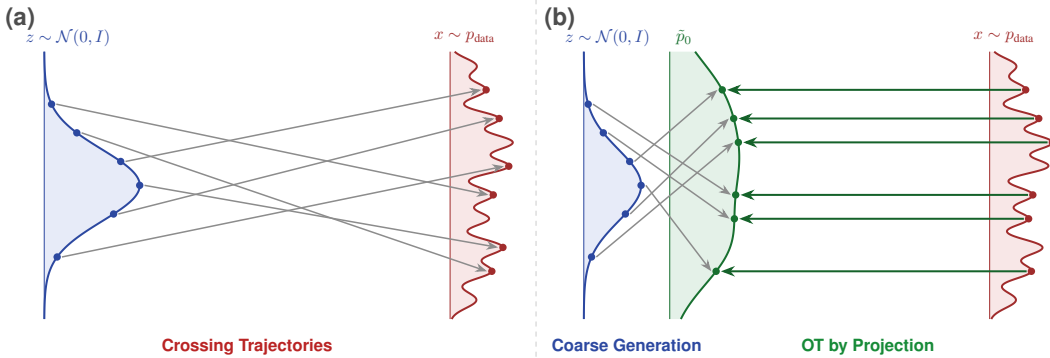


Figure 1: **Why Solve OT When You Can Design It?** (a) Random noise-data pairing in standard flow matching [36] induces crossing trajectories, motivating an OT coupling. (b) Projecting samples onto their low-frequency representation defines an intermediate distribution \tilde{p}_0 whose coupling to the data is OT-optimal by design, while the mapping from Gaussian noise to \tilde{p}_0 reduces to coarse generation.

A number of works have sought to recover what random pairing leaves on the table. Minibatch OT methods [43, 52] solve small transport problems within each training batch, but these local approximations introduce persistent bias that does not vanish with training [28]. To move beyond single-batch scope, some methods accumulate and refine couplings across minibatches throughout training [9], while semi-discrete OT approaches [27, 40] solve a global transport problem over the full dataset as a preprocessing step, adding significant overhead. Distillation [37, 48] and trajectory optimization [54] straighten paths post-training, adding further stages on top of a pretrained model. All of these methods treat the OT problem as something to be solved.

We argue it can be avoided by design, treating the prior itself as a variable to be chosen rather than a fixed input. As illustrated in Fig. 1a, standard flow matching pairs a Gaussian distribution with a complex target through random coupling, producing crossing trajectories that curve the learned velocity field and demand many integration steps at inference. Rather than attempting to solve or approximate the OT coupling for a fixed Gaussian prior, we ask a different question. Can we *choose* a prior distribution for which optimal transport is achieved by design? Concretely, we seek a *new prior distribution*, defined by a transformation of the data, such that the induced coupling is OT-optimal, the new prior can be sampled efficiently and generation from the target distribution remains faithful. Fig. 1b illustrates this idea, where a structured intermediate distribution \tilde{p}_0 replaces the Gaussian. Its coupling to the data is OT-optimal by design, while the remaining mapping from Gaussian noise to \tilde{p}_0 only needs to generate coarse image structure in a lower-dimensional space.

Such a prior can be obtained using a simple, fixed transformation that requires no data-dependent learning or optimization. Leveraging the spectral concentration of natural images [45], we project each image onto its low-frequency representation. Most of the ℓ_2 energy of a natural image lives in its low frequencies, so the projection retains coarse structure while discarding only fine detail. This yields a prior that is informative enough to keep distinct images well separated, and simple enough to be sampled by a lightweight generator. The identity coupling between an image and its low-frequency representation is empirically OT-optimal, recovering an OT pair without solving any OT problem.

This decomposes generation into a low-dimensional problem and an OT-structured one. The first stage operates in a much smaller space, generating only coarse image structure at a fraction of the

original dimensionality. The second stage synthesizes the remaining high-frequency details at full resolution, precisely where the identity coupling between projection and data is OT-optimal by design, requiring no solver or precomputation. A deterministic projection prior lies on a low-dimensional subspace, a known difficulty for velocity-field learning [49]. We interpolate the projection with Gaussian noise, empirically preserving the OT-identity coupling while improving generation quality.

Our contributions are as follows: **(1)** we propose *OT by design*, a new perspective on optimal transport in flow matching. Rather than solving an OT problem for a fixed prior, we design the prior so that its identity coupling to the data is empirically OT-optimal, a property that other methods spend significant effort to approximate. **(2)** We construct this prior using low-frequency projections of training images, verify the resulting identity coupling is OT-optimal with the Hungarian algorithm, add a noise interpolation step that improves generation quality while preserving the coupling, and show that OT-optimality alone is not sufficient without low-frequency structure. **(3)** We show that this design consistently reduces trajectory curvature by more than $2\times$ over existing flow matching methods, yields strong few-step and single-step generation across CIFAR-10, FFHQ, and ImageNet, and integrates naturally with latent-space models, classifier-free guidance, and one-step frameworks such as MeanFlow [13], where it surpasses both the 1-step and 2-step baselines in our experiments.

2 Related work

Flow matching [36, 1, 37] trains continuous normalizing flows [6], enabling simulation-free optimization on linear interpolation paths, and now powers state-of-the-art image synthesis [31, 10]. Pairing noise and data independently during training produces curved generation trajectories [52, 43] that demand many Ordinary Differential Equation (ODE) solver steps at inference. Two complementary lines of work address this, improving the noise-data coupling (Sec. 2.1), and replacing the pure-noise prior with more informative starting distributions (Sec. 2.2). Our work connects them, showing that a simple choice of prior can simultaneously yield OT couplings and straight trajectories.

2.1 Straightening generation trajectories

Minibatch OT coupling. These methods [43, 52] solve an OT problem within each training batch. The resulting coupling is locally straighter but biased [28, 41], and per-batch assignment scales poorly with batch size and dimension [56, 41]. A recent variant [35] selects pairs by model prediction error rather than geometric cost, but remains within single batches.

Global OT coupling. Several methods compute a coupling across the full dataset. One propagates assignments across overlapping batches during training [9], while AlignFlow [27] and SD-FM [40] solve a semi-discrete OT problem offline. These yield higher-quality couplings than minibatch OT, but require dataset-wide precomputation and tie assignments to specific training samples rather than learning a source distribution.

Post-training straightening. A separate line of work straightens trajectories after the base model has been trained, through iterative self-distillation [37], guided distillation [48], or action minimization [54]. These methods are complementary to the choice of coupling and can be applied on top of any training-time method, including ours, to further refine trajectories.

Few-step generation via modified objectives. Consistency models [50, 53], shortcut models [12], and MeanFlow [13] modify the training objective itself for few-step or single-step generation. Because they leave the noise-data coupling unchanged, they are complementary to our prior design and can be composed with it, as we demonstrate by integrating our prior into MeanFlow in Sec. 5.3.

2.2 Alternative priors for generation

The standard isotropic Gaussian prior discards all data structure. A growing body of work replaces or augments this pure-noise prior with degradations that retain partial information about the target. Cold Diffusion [3] showed that purely deterministic degradations such as blur, downsampling, and masking suffice for generation when inverted by a learned model. Subsequent work formalized frequency-aware destruction [19], interpolated between blur and noise [8], and corrupted Fourier magnitude while preserving spatial phase [55]. Anisotropic Gaussians capturing local manifold geometry [2] and time-varying blue noise [20] have similarly been shown to improve flow matching

and diffusion respectively. In the conditional setting, priors reflecting class or prompt structure shorten transport paths [22, 26].

Our work shares this motivation, but rather than designing noise distributions or degradation processes, we show that the choice of prior can be made so that its identity coupling to the data is empirically OT-optimal, yielding an informative starting point and straighter trajectories without solving or approximating an OT problem. Tab. 1 summarizes the properties of these methods, showing that our method operates within the standard flow matching framework without requiring any OT solver.

Table 1: Trade-Offs in Trajectory Straightening. *From Scratch*: no pre-trained model required. *OT-Based*: coupling derived from optimal transport. *Scales w/ B*: no per-batch OT solve. *Scales w/ N*: no dataset-wide precomputation. *Dataset-agnostic*: no assignment tied to training samples.

	From Scratch	OT-Based	Scales w/ batch B	Scales w/ data N	Dataset-agnostic
OT-FM / Multisample FM [52, 43]	✓	✓	✗	✓	✓
OFM [28]	✓	✓	✗	✗	✗
LOOM-CFM [9]	✓	✓	✗	✗	✗
AlignFlow [27]	✓	✓	✓	✗	✗
SD-FM [40]	✓	✓	✓	✗	✗
Lee <i>et al.</i> [34]	✓	✗	✓	✓	✓
Reflow [37]	✗	✗	✓	✓	✓
Conic Reflow [48]	✗	✗	✓	✓	✓
OAT-FM [54]	✗	✓	✓	✓	✓
Ours	✓	✓	✓	✓	✓

3 Background

3.1 Flow matching

Let p_0 and p_1 denote continuous distributions over \mathbb{R}^d , serving as the base (noise) and data distributions, respectively. Flow matching [36, 1, 37] learns a time-dependent flow $\phi_t : \mathbb{R}^d \rightarrow \mathbb{R}^d$ for $t \in [0, 1]$, which maps each sample $x_0 \sim p_0$ along a continuous path such that $\phi_0(x_0) = x_0$ and $\phi_1(x_0) \sim p_1$, *i.e.*, ϕ_1 pushes p_0 forward to p_1 . For brevity, we denote $x_t = \phi_t(x_0)$. The evolution of x_t is governed by an Ordinary Differential Equation (ODE):

$$\frac{d}{dt}x_t = u_t(x_t), \quad (1)$$

where $u_t : \mathbb{R}^d \rightarrow \mathbb{R}^d$, for $t \in [0, 1]$, is the velocity field that generates the flow. The goal of flow matching is to learn a neural velocity field $v_\theta(x_t, t)$ that approximates $u_t(x_t)$.

Directly regressing onto u_t is intractable, but an equivalent *conditional* objective can be optimized instead [36]. Under a linear interpolation path:

$$\phi_t(x_0|x_1) = x_t = tx_1 + (1-t)x_0, \quad (2)$$

where $x_0 \sim p_0, x_1 \sim p_1$ are sampled independently. The corresponding conditional velocity is $u_t(x_t|x_1) = x_1 - x_0$, and the training objective reduces to:

$$\mathcal{L}(\theta) = \mathbb{E}_{t, x_0, x_1} [\|v_\theta(x_t, t) - (x_1 - x_0)\|_2^2], \quad (3)$$

where $t \sim \mathcal{U}[0, 1], x_0 \sim p_0, x_1 \sim p_1$. At inference, new samples are generated by solving the ODE in Eq. (1) from $t = 0$ to $t = 1$, initialized from $x_0 \sim p_0$.

While each conditional velocity $u_t(x_t|x_1) = x_1 - x_0$ defines a straight path between a specific pair (x_0, x_1) , the independent sampling of x_0 and x_1 in Eq. (3) means that these paths may cross one another (Fig. 1a) [13, 43]. The learned velocity field v_θ must average over such conflicting directions, resulting in curved trajectories at inference time. Straightening these trajectories is desirable, as it reduces the number of ODE solver steps required for generation.

3.2 Optimal transport for straightening trajectories

Given a map $T : \mathbb{R}^d \rightarrow \mathbb{R}^d$, we denote the push-forward of p_1 by T as $T_\#(p_1)$, *i.e.*, the distribution of $T(x)$ for $x \sim p_1$. The Monge optimal transport problem seeks a map that transports p_1 to p_0 with minimal squared Euclidean cost:

$$\inf_{T: T_\#(p_1)=p_0} \mathbb{E}_{x_1 \sim p_1} [\|T(x_1) - x_1\|^2]. \quad (4)$$

In the context of flow matching, replacing the independent coupling in Eq. (3) with the OT-optimal pairing eliminates path crossings, since any crossing could be “uncrossed” to reduce the total cost,

contradicting optimality. The resulting velocity field produces significantly straighter trajectories [43, 52], reducing the number of ODE steps needed at inference.

However, computing the OT coupling between a high-dimensional data distribution and a standard Gaussian prior is intractable. While the optimal map is guaranteed to exist [5], obtaining it requires $O(n^3)$ time and $O(n^2)$ memory in the number of samples [30, 7], rendering it infeasible at modern data scales. As discussed in Secs. 1 and 2, existing methods attempt to solve or approximate this coupling at significant cost. Next, we show it can be sidestepped by designing a prior whose identity coupling to the data is OT-optimal by design.

4 Method

Our approach replaces the standard Gaussian prior with a structured distribution obtained by projecting each training image onto its low-frequency representation. Fig. 2 illustrates the full pipeline. We first describe the prior design (Sec. 4.1), then the training and inference procedure (Sec. 4.2).

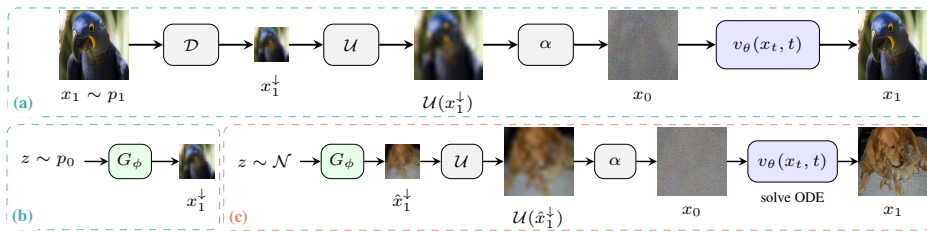


Figure 2: **Full Pipeline.** (a) During **training**, data samples are projected to low frequencies (\mathcal{D}), upsampled (\mathcal{U}), and perturbed with noise (Eq. (5)) to form x_0 , paired with x_1 to train v_θ . (b) G_ϕ is **trained** to map Gaussian noise to the low-frequency distribution. (c) At **inference**, G_ϕ produces a low-frequency sample used to construct a starting point for generation, solving the ODE using v_θ .

4.1 Designing the OT prior

Rather than solving the OT problem for a fixed prior, we treat the prior itself as a design choice. Given the data distribution p_1 , we seek a transformation $T : \mathbb{R}^d \rightarrow \mathbb{R}^d$ that defines the prior as the distribution it induces, $\tilde{p}_0 = T_\#(p_1)$, with two design goals. (i) The identity coupling between data and prior should be OT-optimal, yielding straight, non-crossing trajectories for the flow model. Under the squared-cost OT objective of Eq. (4), the identity coupling pays the mean squared reconstruction error of T , so this goal favors T with small reconstruction error on p_1 . We discuss strict orthogonal projections, for which the identity coupling is exactly OT-optimal, in Sec. C.1, with Sec. D connecting these to the downsampling operators used in the pipeline. (ii) The prior should be expressive enough to support generation of p_1 , yet structured enough to be sampled by a lightweight model at inference. The two goals are not equivalent, and (i) alone is not sufficient, as we show below.

We argue for low-frequency projections of natural images. The power spectrum of natural images follows a $1/f^2$ decay [11, 45], so low-pass filtering retains most of each image’s ℓ_2 energy and incurs only small reconstruction error, addressing goal (i). The resulting prior consists of low-resolution images capturing coarse structure, simple enough for a lightweight model to sample, addressing (ii).

To check that the two goals are genuinely independent, we compare four projection variants for T . Fourier truncation, random pixel masking, and random patch masking are strict orthogonal projections and therefore provably preserve the OT-identity coupling (Prop. D.2). Only the low-frequency variants yield low FID and low trajectory curvature under noise perturbation (Tab. C.3). OT-optimality of the identity coupling is therefore not sufficient, the prior must also retain low-frequency structure that a lightweight model can sample efficiently. Among the low-frequency variants, bicubic downsampling yields a small but consistent FID improvement over Fourier truncation, and we adopt it.

The resulting design relates to a recurring principle in generative modeling. Cascaded diffusion [17, 47], latent diffusion [44], and pyramid flow [23] all decompose generation across resolutions or feature scales, generating coarse structure first and refining it with high-frequency detail. Our

contribution is to make this decomposition explicit at the level of the flow’s coupling. The flow model never has to invent coarse structure, its starting point already contains it, and the residual task of synthesizing high-frequency detail is exactly the regime where the OT-identity coupling holds.

The deterministic coupling defined by T pairs each x_1 with a single fixed $T(x_1)$. While this is the exact coupling we sought, the resulting prior concentrates on a low-dimensional subspace, where nearby prior samples can be matched to distant data points. The velocity field is then forced to average over conflicting transport directions within small neighborhoods, producing curved trajectories at inference time. This echoes the observation in score-based generative modeling [49] that learning a stable vector field over data concentrated on a low-dimensional manifold is difficult. Deterministic coupling also exposes the model to the same pair $(T(x_1), x_1)$ every epoch, risking overfitting. Adding noise alleviates both issues by spreading the prior and breaking the pairing. We formalize this by interpolating the low-frequency representation and Gaussian noise:

$$x_0 = (1 - \alpha)T(x_1) + \alpha \epsilon, \quad \epsilon \sim \mathcal{N}(0, I), \quad (5)$$

where $\alpha \in [0, 1]$ controls the noise ratio. $\alpha = 0$ recovers the deterministic coupling, and $\alpha = 1$ reduces to standard flow matching with random pairings.

The expected squared distance between two noisy prior samples decomposes as

$$\mathbb{E} [\|x_0^{(i)} - x_0^{(j)}\|^2] = (1 - \alpha)^2 \mathbb{E} [\|T(x_1^{(i)}) - T(x_1^{(j)})\|^2] + \alpha^2 \mathbb{E} [\|\epsilon_i - \epsilon_j\|^2]. \quad (6)$$

The first term is the mean pairwise distance in the projected subspace, while the second evaluates to $2\alpha^2 d$, growing linearly with the data dimensionality, so even moderate noise levels provide substantial separation between prior samples (Fig. B.3b).

A natural question is whether the OT-identity coupling survives noise interpolation. To test this, we compute the exact discrete OT assignment (Hungarian algorithm) between 10,000 noisy prior samples and their corresponding data samples at different noise levels, and measure the fraction of pairs whose optimal assignment matches the identity coupling. Fig. 3 shows that the identity coupling remains OT-optimal up to $\alpha \approx 0.5$ (shown as 50% noise ratio in the figure), in both pixel space (CIFAR-10, 99.9% preservation) and latent space (FFHQ, 100%), with the sample images above the bars showing progression in α . Only beyond $\alpha = 0.5$ does noise disrupt the assignment structure. Sec. B.1 extends this analysis with a finer α sweep and the full derivation of Eq. (6).

Moderate noise preserves the OT coupling and improves generation quality, with FID minimized near $\alpha = 0.5$. Quality improves steadily from $\alpha = 0$ to $\alpha = 0.5$, then degrades as noise overwhelms the low-frequency structure. At lower values, prior samples cluster tightly in the projected subspace, risking overfitting and trajectory crossings. The $\alpha = 0$ endpoint is itself a meaningful baseline, a pure coarse-to-fine pipeline in which v_θ refines a deterministic projection prior without any noise interpolation. The FID gap to $\alpha = 0.5$ in Fig. B.3a thus measures the contribution of the OT-preserving noise interpolation beyond a coarse-to-fine substrate alone. We adopt $\alpha = 0.5$ as the operating point for all our experiments (full FID sweep in Fig. B.3a).

4.2 Pipeline and training

We instantiate $T = \mathcal{U} \circ \mathcal{D}$, where $\mathcal{D}: \mathbb{R}^d \rightarrow \mathbb{R}^{d'}$ produces $x_1^\downarrow = \mathcal{D}(x_1) \in \mathbb{R}^{d'}$, and $\mathcal{U}: \mathbb{R}^{d'} \rightarrow \mathbb{R}^d$ is its corresponding upsampling, so that T maps x_1 to its low-frequency approximation in \mathbb{R}^d . During training (Fig. 2a), $T(x_1)$ is computed directly from each data sample and perturbed via Eq. (5) to form the starting point x_0 , which is paired with x_1 for standard flow matching training of v_θ (see Alg. A.1). At inference (Fig. 2c), a lightweight generator G_ϕ maps Gaussian noise to $\mathbb{R}^{d'}$. In practice, G_ϕ is

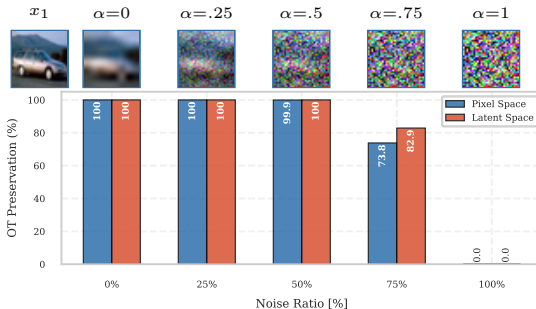


Figure 3: **OT Preservation Under Noise.** Fraction of pairs whose optimal assignment matches the identity coupling, in *pixel space* (CIFAR-10) and *latent space* (FFHQ). Above the bars: a sample at each noise level.

itself a flow matching model operating at a small fraction of the original dimensionality (architecture details in Sec. 5), trained separately (Fig. 2b) to produce \hat{x}_1^\downarrow , which is deterministically upsampled to $\mathcal{U}(\hat{x}_1^\downarrow)$ and perturbed with noise. The flow model v_θ , under the OT-identity coupling, synthesizes the remaining high-frequency details, with no OT problem to solve and no architectural changes.

5 Experiments

5.1 Experimental setup

Datasets. We evaluate on three benchmarks of increasing complexity: CIFAR-10 [29] (32×32), FFHQ [25] (256×256), and ImageNet [46] (256×256). CIFAR-10 is trained in pixel space, following the architecture and training recipe of Tong *et al.* [52], while for the 256×256 datasets, we follow standard practice and train using the SiT architecture [13, 38], and operate in the latent space of a pretrained auto-encoder [44], yielding $32 \times 32 \times 4$ latents. We downsample by $4 \times$ per spatial dimension, producing an 8×8 low-frequency prior. G_ϕ is trained on a smaller variant of the same architecture family for each experiment, and operates on these representations. Full architectural details, training procedures, low-frequency projection specifications, and ablations are provided in Secs. A and C.

Baselines. We compare against IFM [36] (independent coupling), OT-FM [52] (minibatch OT), and AlignFlow [27] (semi-discrete OT). All baselines are single-network models, and our flow model v_θ uses the same architecture and parameter count as theirs. The additional cost of the lightweight G_ϕ is reported through the effective NFE, with full details in Tabs. A.1 and A.2 and Sec. A.1. On ImageNet we evaluate with classifier-free guidance (CFG) [16] and integrate our prior into MeanFlow [13], a one-step generation framework.

Evaluation. We report FID [15] for generation quality (log scale in all plots), and curvature [43, 34], which quantifies how close the learned trajectories are to straight lines. Our two-stage pipeline incurs a small overhead from the lightweight generator G_ϕ . In wall-clock time, one G_ϕ step takes $\approx 0.09 \times$ the time of a main-model step. We use 8 generation steps for G_ϕ in all experiments (Sec. C.3) and report *effective NFE* throughout, accounting for both stages. For example, 1 main-model step yields an effective NFE of 1.72. We additionally report results with a single G_ϕ step (effective NFE overhead of only 0.09) to demonstrate robustness to the prior-generation budget, and Sec. B.2 provides the perfect-prior upper bound. Together these bracket the sensitivity of final FID to G_ϕ quality. We use $\alpha = 0.5$ throughout, as motivated in Sec. 4.1. At inference, we additionally apply a small noise perturbation to x_0 , see Sec. A.4 for details.

5.2 Pixel space (CIFAR-10)

We begin with CIFAR-10 in pixel space. Fig. 4a plots FID vs NFE for IFM [36], OT-FM [52], AlignFlow [27], and our method. Note that our effective NFE takes into account the cost of running

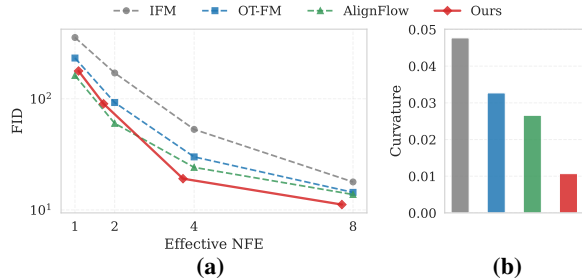


Figure 4: **CIFAR-10 Results.** Our method achieves lower FID (\downarrow) across most step counts (a) and at least $2 \times$ lower curvature (\downarrow) than the next best baseline (b).

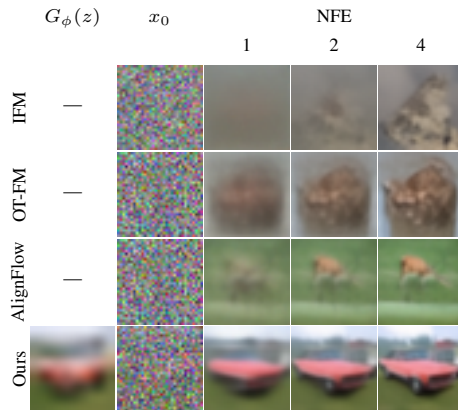


Figure 5: **CIFAR-10 Generation.** Samples generated at 1, 2, and 4 NFE. For our method NFE counts v_θ evaluations. $G_\phi(z)$ is the generated low-frequency sample and x_0 the noised starting point. All baselines start from Gaussian noise.

G_ϕ . At all comparison points beyond the first, our method uses fewer total function evaluations than the baselines. Our method outperforms IFM and OT-FM across all step counts. Compared to AlignFlow, which requires a preprocessing stage to solve a semi-discrete OT problem over the full dataset, our method achieves better FID at 4 and 8 effective NFE. As the number of steps increases, all methods converge, confirming the advantage of trajectory straightening is concentrated in the few-step regime. We additionally report results with a single G_ϕ step (effective NFE of 1.09), demonstrating competitive performance even in this minimal-cost setting. Fig. 4b explains this improvement through trajectory curvature. Our method achieves substantially lower curvature than all baselines, at least $2\times$ below AlignFlow, the second-best method, and $4\times$ lower than IFM.

Fig. 5 provides qualitative support. At 1 NFE, baselines produce visibly blurred outputs of varying quality, as the velocity field must compress curved trajectories into a single step. Our method, starting from a structured low-frequency prior (x_0 column), already captures the coarse layout of the target image, and a single step suffices to synthesize recognizable content. By 4 NFE, our samples exhibit clear object structure and color fidelity, while the baselines remain noticeably degraded.

5.3 Latent space (FFHQ & ImageNet)

Fig. 6a reports FID as a function of effective NFE on FFHQ 256×256 . Our method achieves the best FID at all step counts except NFE = 2, where our effective cost is only 1.72 steps. The gains are largest at 1 step, with 20% improvement over OT-FM and 38% over IFM. AlignFlow [27] is excluded from latent-space experiments, as it requires precomputed OT assignments only publicly available for CIFAR-10. Fig. 6b shows the mechanism behind these improvements. Our method reduces curvature to 0.083, under half of OT-FM (0.172) and less than 42% of IFM (0.201). This confirms that our approach extends to latent space, where the OT-identity coupling holds for the latent representations under Hungarian verification (Fig. 3).

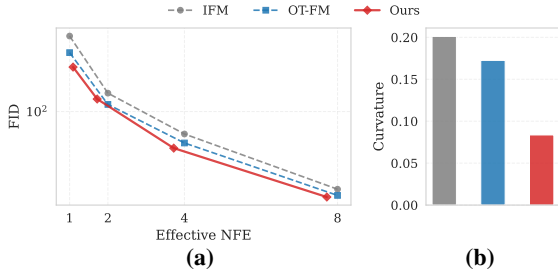


Figure 6: **FFHQ Results.** (a) Our method achieves lower FID (\downarrow) across all steps but 2. (b) Our method achieves at least $2\times$ lower curvature (\downarrow) than the next best baseline.

Fig. 7 compares samples generated at 2 NFE across all three methods. Notably, our method uses an effective NFE of only 1.72 at this setting, yet the visual comparison reveals a clear advantage. IFM and OT-FM produce faces with noticeable artifacts and incomplete facial structure. Our method generates more coherent samples with significantly fewer artifacts, reflecting the advantage of starting from a structured prior that already captures the coarse layout.

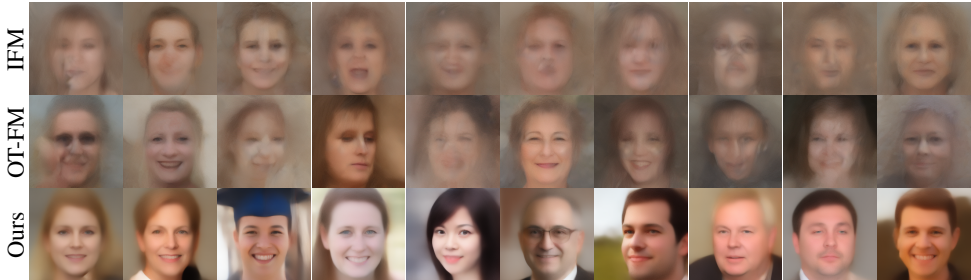


Figure 7: **FFHQ 2-NFE generation.** Baselines use 2 NFE, while our method uses an effective NFE of only 1.72, fewer than the baselines.

ImageNet and Classifier-Free Guidance. To evaluate scaling to larger datasets, we train the same SiT backbone on class-conditional ImageNet 256×256 . Due to compute constraints, we train for the same number of iterations used in our other experiments rather than to full convergence, so absolute FID values are higher than those of fully trained models. The comparison is nonetheless informative, as both methods share the same architecture and training budget. Tab. 2 reports FID and curvature at 1 NFE (1.09 effective for our method). Since training is partial, absolute FID values are high;

nevertheless, relative improvements are informative. Our method lowers FID from 314.80 to 248.42 with CFG and from 322.18 to 268.14 without CFG, yielding even larger gains in the guided setting. Curvature is reduced by more than $2.3\times$ compared to IFM in both configurations, suggesting that the straighter trajectories observed on FFHQ extend to a large scale dataset such as ImageNet. Our approach integrates with classifier-free guidance [16], as both G_ϕ and the main model are trained with the standard CFG scheme. The FID improvement holds in both settings, confirming that our approach complements CFG rather than substituting for it.

One-Step Generation with MeanFlow. MeanFlow [13] is a one-step generation framework that trains from scratch by modeling average rather than instantaneous velocity, requiring no distillation or curriculum learning. We integrate our prior into MeanFlow and evaluate on ImageNet 256×256 , following the setup of Tab. 1 in the original paper [13]. We use the pretrained checkpoint from a popular PyTorch reproduction [57] as our baseline, which achieves better FID than the original paper, and train our variant from scratch using the same codebase. As shown in Tab. 3, our method outperforms MeanFlow at both 1 and 2 steps using only 1.72 effective NFE, while reducing curvature by $2.3\times$, confirming that our prior yields substantially straighter trajectories even in a framework already optimized for one-step generation. This integration illustrates how our prior complements training-objective changes such as consistency models [50, 53] and distillation [37, 48], which modify the learning objective while our method modifies the coupling the velocity field is trained on.

Ablations. We ablate the projection operator (Sec. C.1), the downsampling factor (Sec. C.2), and the G_ϕ step count (Sec. C.3), the first showing that low-frequency structure is the necessary ingredient beyond OT-optimality alone.

Table 2: **ImageNet CFG Results.** FID and curvature at 1 NFE (1.09 effective for our method). High FIDs reflect partial training.

	Method	FID (\downarrow)	Curv. (\downarrow)
w/o CFG	IFM	322.18	0.227
	Ours	268.14	0.097
w/ CFG	IFM	314.80	0.223
	Ours	248.42	0.095

Table 3: **MeanFlow on ImageNet.** FID and curvature at low-NFE. High FIDs reflect partial training.

Method	NFE	FID (\downarrow)	Curv. (\downarrow)
MeanFlow	1	59.07	0.221
	2	55.40	
MeanFlow + Ours	1.72	54.66	0.097

6 Limitations and conclusion

Prior generation. Our empirical OT-identity coupling applies to the flow from \tilde{p}_0 to the data, but not to generating \tilde{p}_0 itself, as G_ϕ is trained under independent coupling, so the entire pipeline is not fully OT-coupled. This adds only a small inference overhead in practice, since low-frequency natural-image distributions are smooth and concentrated (Sec. 4), making them easier to generate [17]. At the same time, G_ϕ remains the main bottleneck: in an oracle CIFAR-10 experiment, replacing G_ϕ with true low-frequency projections of training images improves FID at 1 NFE from 90.16 to 28.12. Since G_ϕ is decoupled from v_θ , improving it should directly improve the full pipeline (see Sec. B.2).

Domain specificity. Our prior uses low-frequency projections, which empirically preserve the OT-identity coupling for natural images because their spectrum is concentrated at low frequencies [45], keeping projected samples well separated. This property also carries over to VAE latents (Sec. 5.3) and holds for structured datasets such as FFHQ. For other modalities, whether an analogous projection preserves the OT-identity coupling depends on the data geometry and should be examined per domain.

Overall, our results show that OT couplings for flow matching can be obtained not only by solving an OT problem, but also by designing a suitable prior. Replacing the Gaussian prior with low-frequency projections yields an empirically OT-optimal identity coupling, straighter trajectories, and improved few-step generation quality, while integrating naturally with latent-space models, classifier-free guidance, and one-step generation frameworks.

7 Acknowledgements

This project was partially supported by ISF grants 1574/21 and 2132/23.

References

- [1] Michael S Albergo and Eric Vanden-Eijnden. Building normalizing flows with stochastic interpolants. *arXiv preprint arXiv:2209.15571*, 2022.
- [2] Jacob Bamberger, Iolo Jones, Dennis Duncan, Michael M Bronstein, Pierre Vandergheynst, and Adam Gosztolai. Carré du champ flow matching: better quality-generalisation tradeoff in generative models. *arXiv preprint arXiv:2510.05930*, 2025.
- [3] Arpit Bansal, Eitan Borgnia, Hong-Min Chu, Jie S. Li, Hamid Kazemi, Furong Huang, Micah Goldblum, Jonas Geiping, and Tom Goldstein. Cold diffusion: Inverting arbitrary image transforms without noise. In *Thirty-seventh Conference on Neural Information Processing Systems*, 2023. URL <https://openreview.net/forum?id=XH3ArcctI>.
- [4] Zalán Borsos, Raphaël Marinier, Damien Vincent, Eugene Kharitonov, Olivier Pietquin, Matt Sharifi, Dominik Roblek, Olivier Teboul, David Grangier, Marco Tagliasacchi, et al. Audioldm: a language modeling approach to audio generation. *IEEE/ACM transactions on audio, speech, and language processing*, 31:2523–2533, 2023.
- [5] Yann Brenier. Polar factorization and monotone rearrangement of vector-valued functions. *Communications on pure and applied mathematics*, 44(4):375–417, 1991.
- [6] Ricky TQ Chen, Yulia Rubanova, Jesse Bettencourt, and David K Duvenaud. Neural ordinary differential equations. *Advances in neural information processing systems*, 31, 2018.
- [7] Marco Cuturi. Sinkhorn distances: Lightspeed computation of optimal transport. In C.J. Burges, L. Bottou, M. Welling, Z. Ghahramani, and K.Q. Weinberger, editors, *Advances in Neural Information Processing Systems*, volume 26. Curran Associates, Inc., 2013. URL https://proceedings.neurips.cc/paper_files/paper/2013/file/af21d0c97db2e27e13572cbf59eb343d-Paper.pdf.
- [8] Giannis Daras, Mauricio Delbracio, Hossein Talebi, Alex Dimakis, and Peyman Milanfar. Soft diffusion: Score matching with general corruptions. *Transactions on Machine Learning Research*, 2023. ISSN 2835-8856. URL <https://openreview.net/forum?id=W98rebBxlQ>.
- [9] Aram Davtyan, Leello Tadesse Dadi, Volkan Cevher, and Paolo Favaro. Faster inference of flow-based generative models via improved data-noise coupling. In *The Thirteenth International Conference on Learning Representations*, 2025.
- [10] Patrick Esser, Sumith Kulal, Andreas Blattmann, Rahim Entezari, Jonas Müller, Harry Saini, Yam Levi, Dominik Lorenz, Axel Sauer, Frederic Boesel, et al. Scaling rectified flow transformers for high-resolution image synthesis. In *Forty-first international conference on machine learning*, 2024.
- [11] David J Field. Relations between the statistics of natural images and the response properties of cortical cells. *Journal of the Optical Society of America A*, 4(12):2379–2394, 1987.
- [12] Kevin Frans, Danijar Hafner, Sergey Levine, and Pieter Abbeel. One step diffusion via shortcut models. In *The Thirteenth International Conference on Learning Representations*, 2025. URL <https://openreview.net/forum?id=0lzB6LnXcS>.
- [13] Zhengyang Geng, Mingyang Deng, Xingjian Bai, J Zico Kolter, and Kaiming He. Mean flows for one-step generative modeling. In *The Thirty-ninth Annual Conference on Neural Information Processing Systems*, 2025. URL <https://openreview.net/forum?id=uWj4s7rMnR>.
- [14] Yoav HaCohen, Nisan Chiprut, Benny Brazowski, Daniel Shalem, Dudu Moshe, Eitan Richardson, Eran Levin, Guy Shiran, Nir Zabari, Ori Gordon, et al. Ltx-video: Realtime video latent diffusion. *arXiv preprint arXiv:2501.00103*, 2024.

- [15] Martin Heusel, Hubert Ramsauer, Thomas Unterthiner, Bernhard Nessler, and Sepp Hochreiter. Gans trained by a two time-scale update rule converge to a local nash equilibrium. *Advances in neural information processing systems*, 30, 2017.
- [16] Jonathan Ho and Tim Salimans. Classifier-free diffusion guidance. *arXiv preprint arXiv:2207.12598*, 2022.
- [17] Jonathan Ho, Chitwan Saharia, William Chan, David J Fleet, Mohammad Norouzi, and Tim Salimans. Cascaded diffusion models for high fidelity image generation. *Journal of Machine Learning Research*, 23(47):1–33, 2022.
- [18] Jonathan Ho, Tim Salimans, Alexey A. Gritsenko, William Chan, Mohammad Norouzi, and David J. Fleet. Video diffusion models. In Alice H. Oh, Alekh Agarwal, Danielle Belgrave, and Kyunghyun Cho, editors, *Advances in Neural Information Processing Systems*, 2022. URL https://openreview.net/forum?id=f3zNgKga_ep.
- [19] Emiel Hoogeboom and Tim Salimans. Blurring diffusion models. In *The Eleventh International Conference on Learning Representations*, 2023. URL <https://openreview.net/forum?id=0jDkC57x5sz>.
- [20] Xingchang Huang, Corentin Salaun, Cristina Vasconcelos, Christian Theobalt, Cengiz Oztireli, and Gurprit Singh. Blue noise for diffusion models. In *ACM SIGGRAPH 2024 conference papers*, pages 1–11, 2024.
- [21] Ka-Hei Hui, Chao Liu, Xiaohui Zeng, Chi-Wing Fu, and Arash Vahdat. Not-so-optimal transport flows for 3d point cloud generation. In *The Thirteenth International Conference on Learning Representations*, 2025. URL <https://openreview.net/forum?id=62Ff8LDAJZ>.
- [22] Noam Issachar, Mohammad Salama, Raanan Fattal, and Sagie Benaim. Designing a conditional prior distribution for flow-based generative models. *arXiv preprint arXiv:2502.09611*, 2025.
- [23] Yang Jin, Zhicheng Sun, Ningyuan Li, Kun Xu, Kun Xu, Hao Jiang, Nan Zhuang, Quzhe Huang, Yang Song, Yadong MU, and Zhouchen Lin. Pyramidal flow matching for efficient video generative modeling. In *The Thirteenth International Conference on Learning Representations*, 2025. URL <https://openreview.net/forum?id=66NzcrQuOq>.
- [24] Bowen Jing, Bonnie Berger, and Tommi Jaakkola. Alphafold meets flow matching for generating protein ensembles. In *NeurIPS 2023 Generative AI and Biology (GenBio) Workshop*, 2023. URL <https://openreview.net/forum?id=yQcebEgQfH>.
- [25] Tero Karras, Samuli Laine, and Timo Aila. A style-based generator architecture for generative adversarial networks. In *Proceedings of the IEEE/CVF conference on computer vision and pattern recognition*, pages 4401–4410, 2019.
- [26] Junwan Kim, Jiho Park, Seonghu Jeon, and Seungryong Kim. Better source, better flow: Learning condition-dependent source distribution for flow matching. *arXiv preprint arXiv:2602.05951*, 2026.
- [27] Lingkai Kong, Molei Tao, Yang Liu, Bryan Wang, Jinmiao Fu, Chien-Chih Wang, and Huidong Liu. Alignflow: Improving flow-based generative models with semi-discrete optimal transport. *arXiv preprint arXiv:2510.15038*, 2025.
- [28] Nikita Kornilov, Petr Mokrov, Alexander Gasnikov, and Aleksandr Korotin. Optimal flow matching: Learning straight trajectories in just one step. *Advances in Neural Information Processing Systems*, 37:104180–104204, 2024.
- [29] Alex Krizhevsky, Geoffrey Hinton, et al. Learning multiple layers of features from tiny images. Technical report, University of Toronto, 2009.
- [30] Harold W Kuhn. The hungarian method for the assignment problem. *Naval research logistics quarterly*, 2(1-2):83–97, 1955.
- [31] Black Forest Labs. Flux. <https://github.com/black-forest-labs/flux>, 2024.

- [32] Yushi LAN, Shangchen Zhou, Zhaoyang Lyu, Fangzhou Hong, Shuai Yang, Bo Dai, Xingang Pan, and Chen Change Loy. Gaussiananything: Interactive point cloud flow matching for 3d generation. In *The Thirteenth International Conference on Learning Representations*, 2025. URL <https://openreview.net/forum?id=P4DbTSDQFu>.
- [33] Matthew Le, Apoorv Vyas, Bowen Shi, Brian Karrer, Leda Sari, Rashed Moritz, Mary Williamson, Vimal Manohar, Yossi Adi, Jay Mahadeokar, and Wei-Ning Hsu. Voicebox: Text-guided multilingual universal speech generation at scale. In A. Oh, T. Naumann, A. Globerson, K. Saenko, M. Hardt, and S. Levine, editors, *Advances in Neural Information Processing Systems*, volume 36, pages 14005–14034. Curran Associates, Inc., 2023. URL https://proceedings.neurips.cc/paper_files/paper/2023/file/2d8911db9ecedf866015091b28946e15-Paper-Conference.pdf.
- [34] Sangyun Lee, Beomsu Kim, and Jong Chul Ye. Minimizing trajectory curvature of ode-based generative models. In *International Conference on Machine Learning*, pages 18957–18973. PMLR, 2023.
- [35] Yexiong Lin, Yu Yao, and Tongliang Liu. Beyond optimal transport: Model-aligned coupling for flow matching, 2025. URL <https://arxiv.org/abs/2505.23346>.
- [36] Yaron Lipman, Ricky TQ Chen, Heli Ben-Hamu, Maximilian Nickel, and Matt Le. Flow matching for generative modeling. *arXiv preprint arXiv:2210.02747*, 2022.
- [37] Xingchao Liu, Chengyue Gong, and Qiang Liu. Flow straight and fast: Learning to generate and transfer data with rectified flow. *arXiv preprint arXiv:2209.03003*, 2022.
- [38] Nanye Ma, Mark Goldstein, Michael S Albergo, Nicholas M Boffi, Eric Vanden-Eijnden, and Saining Xie. Sit: Exploring flow and diffusion-based generative models with scalable interpolant transformers. In *European Conference on Computer Vision*, pages 23–40. Springer, 2024.
- [39] Shivam Mehta, Ruibo Tu, Jonas Beskow, Éva Székely, and Gustav Eje Henter. Matcha-tts: A fast tts architecture with conditional flow matching. In *ICASSP 2024-2024 IEEE International Conference on Acoustics, Speech and Signal Processing (ICASSP)*, pages 11341–11345. IEEE, 2024.
- [40] Alireza Mousavi-Hosseini, Stephen Y Zhang, Michal Klein, and Marco Cuturi. Flow matching with semidiscrete couplings. *arXiv preprint arXiv:2509.25519*, 2025.
- [41] Alireza Mousavi-Hosseini, Stephen Y. Zhang, Michal Klein, and marco cuturi. On fitting flow models with large sinkhorn couplings. In *NeurIPS 2025 Workshop on Structured Probabilistic Inference & Generative Modeling*, 2025. URL <https://openreview.net/forum?id=0hCgpYn1Pu>.
- [42] Adam Polyak, Amit Zohar, Andrew Brown, Andros Tjandra, Animesh Sinha, Ann Lee, Apoorv Vyas, Bowen Shi, Chih-Yao Ma, Ching-Yao Chuang, et al. Movie gen: A cast of media foundation models. *arXiv preprint arXiv:2410.13720*, 2024.
- [43] Aram-Alexandre Pooladian, Heli Ben-Hamu, Carles Domingo-Enrich, Brandon Amos, Yaron Lipman, and Ricky TQ Chen. Multisample flow matching: Straightening flows with minibatch couplings. *arXiv preprint arXiv:2304.14772*, 2023.
- [44] Robin Rombach, Andreas Blattmann, Dominik Lorenz, Patrick Esser, and Björn Ommer. High-resolution image synthesis with latent diffusion models. In *Proceedings of the IEEE/CVF conference on computer vision and pattern recognition*, pages 10684–10695, 2022.
- [45] Daniel L Ruderman. The statistics of natural images. *Network: computation in neural systems*, 5(4):517, 1994.
- [46] Olga Russakovsky, Jia Deng, Hao Su, Jonathan Krause, Sanjeev Satheesh, Sean Ma, Zhiheng Huang, Andrej Karpathy, Aditya Khosla, Michael Bernstein, et al. Imagenet large scale visual recognition challenge. *International journal of computer vision*, 115(3):211–252, 2015.

- [47] Chitwan Saharia, William Chan, Saurabh Saxena, Lala Li, Jay Whang, Emily L Denton, Kamyar Ghasemipour, Raphael Gontijo Lopes, Burcu Karagol Ayan, Tim Salimans, et al. Photorealistic text-to-image diffusion models with deep language understanding. *Advances in neural information processing systems*, 35:36479–36494, 2022.
- [48] Shin seong Kim, Mingi Kwon, Jaeseok Jeong, and Youngjung Uh. Balanced conic rectified flow. In *The Thirty-ninth Annual Conference on Neural Information Processing Systems*, 2025.
- [49] Yang Song and Stefano Ermon. Generative modeling by estimating gradients of the data distribution. *Advances in neural information processing systems*, 32, 2019.
- [50] Yang Song, Prafulla Dhariwal, Mark Chen, and Ilya Sutskever. Consistency models. In Andreas Krause, Emma Brunskill, Kyunghyun Cho, Barbara Engelhardt, Sivan Sabato, and Jonathan Scarlett, editors, *Proceedings of the 40th International Conference on Machine Learning*, volume 202 of *Proceedings of Machine Learning Research*, pages 32211–32252. PMLR, 23–29 Jul 2023. URL <https://proceedings.mlr.press/v202/song23a.html>.
- [51] Yuxuan Song, Jingjing Gong, Minkai Xu, Ziyao Cao, Yanyan Lan, Stefano Ermon, Hao Zhou, and Wei-Ying Ma. Equivariant flow matching with hybrid probability transport for 3d molecule generation. In *Thirty-seventh Conference on Neural Information Processing Systems*, 2023. URL <https://openreview.net/forum?id=hHUZ5V9XFu>.
- [52] Alexander Tong, Kilian FATRAS, Nikolay Malkin, Guillaume Huguet, Yanlei Zhang, Jarrid Rector-Brooks, Guy Wolf, and Yoshua Bengio. Improving and generalizing flow-based generative models with minibatch optimal transport. *Transactions on Machine Learning Research*, 2024. ISSN 2835-8856. URL <https://openreview.net/forum?id=CD9Snc73AW>. Expert Certification.
- [53] Ling Yang, Zixiang Zhang, Zhilong Zhang, Xingchao Liu, Minkai Xu, Wentao Zhang, Chenlin Meng, Stefano Ermon, and Bin Cui. Consistency flow matching: Defining straight flows with velocity consistency. *arXiv preprint arXiv:2407.02398*, 2024.
- [54] Angxiao Yue, Anqi Dong, and Hongteng Xu. Oat-fm: Optimal acceleration transport for improved flow matching. *arXiv preprint arXiv:2509.24936*, 2025.
- [55] Yu Zeng, Charles Ochoa, Mingyuan Zhou, Vishal M Patel, Vitor Guizilini, and Rowan McAllister. Neuralremaster: Phase-preserving diffusion for structure-aligned generation. *arXiv preprint arXiv:2512.05106*, 2025.
- [56] Stephen Zhang, Alireza Mousavi-Hosseini, Michal Klein, and Marco Cuturi. On fitting flow models with large sinkhorn couplings. *arXiv preprint arXiv:2506.05526*, 2025.
- [57] Yu Zhu. Meanflow: Pytorch implementation. <https://github.com/zhuyu-cs/MeanFlow>, 2025. PyTorch implementation of Mean Flows for One-step Generative Modeling.

Appendices

We provide implementation details (Sec. A), empirical validation of the OT coupling (Sec. B), ablation studies (Sec. C), formal proofs (Sec. D), and qualitative results (Sec. E).

A Implementation details

A.1 Architecture and training

Table A.1: **CIFAR-10 Architecture and Training.** Models share the UNet backbone, as prior work [36, 52], differing only in capacity (bottom block).

<i>Shared architecture</i>		
Architecture	UNet	
Base channels	128	
Res. blocks / level	2	
Attn. heads	4 (64 dim/hd)	
Dropout	0.1	
<i>Shared training</i>		
Optimizer	Adam (2×10^{-4})	
LR warmup	5k (linear)	
Batch size	128	
Total steps	400k	
EMA decay	0.9999	
Grad. clip	1.0	
Augmentation	Horiz. flip	
	v_θ	G_ϕ
Input res.	$32^2 \times 3$	$8^2 \times 3$
Chan. mult.	[1,2,2,2]	[1,2]
Attn. res.	16	4
Parameters	~ 36 M	~ 10 M

Table A.2: **256×256 Architecture and Training.** All setups share SiT [38] backbones for v_θ and G_ϕ . MeanFlow adds dual time embedding (r, t).

<i>Shared training</i>			
Optimizer	AdamW (1×10^{-4} , const.)		
EMA decay	0.9999		
	v_θ (B/4)	G_ϕ (S/2)	
Depth/hid./heads	12/768/12	12/384/6	
Patch / tokens	4 / 64	2 / 16	
Input	$32^2 \times 4$	$8^2 \times 4$	
Parameters	~ 130 M	~ 33 M	
	<i>FFHQ</i>	<i>ImageNet</i>	<i>MeanFlow</i>
Time emb.	Single (t)	Dual (r, t)	
Betas	(.9, .999)	(.9, .95)	
Time sampler	Uniform	Logit-norm.	
$r \neq t$ ratio	—	0.25	
Grad. clip	—	1.0	
Batch size	256	1024	256
Epochs	1400	80	80
Steps	380k	100k	400k

CIFAR-10. Tab. A.1 lists the architecture and training configuration for CIFAR-10 (Sec. 5.2). We train IFM [36], OT-FM [52], AlignFlow [27], and our method from scratch, except that for AlignFlow we additionally use the pretrained assignment model from the official repository.

Algorithm A.1 Training and Inference.

Hyperparameters: noise ratio $\alpha = 0.5$, downsampling factor $k = 4$

▷ **Training: construct OT-structured pairs**

```
1: function BUILDCOUPLING( $x_1$ )
2:    $x_1^\downarrow \leftarrow \text{F.interpolate}(x_1, \text{scale\_factor}=1/k, \text{mode}=\text{"area"})$ 
3:    $\mathcal{U}(x_1^\downarrow) \leftarrow \text{F.interpolate}(x_1^\downarrow, \text{scale\_factor}=k, \text{mode}=\text{"bicubic"})$ 
4:    $\epsilon \leftarrow \text{torch.randn\_like}(\mathcal{U}(x_1^\downarrow))$ 
5:    $x_0 \leftarrow (1 - \alpha)\mathcal{U}(x_1^\downarrow) + \alpha \epsilon$  ▷ Eq. (5)
6:   return  $x_0$ 
7: end function
```

▷ **Training loop**

```
8: for  $x_1 \sim p_1$  do
9:    $x_0 \leftarrow \text{BUILDCOUPLING}(x_1)$ 
10:   $t \leftarrow \text{torch.rand}(1)$ 
11:   $x_t \leftarrow t x_1 + (1 - t) x_0$  ▷ Eq. (2)
12:   $\mathcal{L} \leftarrow \|v_\theta(x_t, t) - (x_1 - x_0)\|^2$  ▷ Eq. (3)
13:  Update  $\theta$ 
14: end for
```

▷ **Inference**

```
15: function GENERATE( $G_\phi, v_\theta$ )
16:   $z \leftarrow \text{torch.randn}(\dots)$  ▷ sample Gaussian noise
17:   $\hat{x}_1^\downarrow \leftarrow G_\phi(z)$  ▷ generate low-frequency sample
18:   $\mathcal{U}(\hat{x}_1^\downarrow) \leftarrow \text{F.interpolate}(\hat{x}_1^\downarrow, \text{scale\_factor}=k, \text{mode}=\text{"bicubic"})$ 
19:   $\epsilon \leftarrow \text{torch.randn\_like}(\mathcal{U}(\hat{x}_1^\downarrow))$ 
20:   $\tilde{x}_0 \leftarrow (1 - \alpha)\mathcal{U}(\hat{x}_1^\downarrow) + \alpha \epsilon$ 
21:   $x_1 \leftarrow \text{ODESOLVE}(v_\theta, \tilde{x}_0, t=0 \rightarrow 1)$ 
22:  return  $x_1$ 
23: end function
```

FFHQ, ImageNet, and MeanFlow. Tab. A.2 lists the configuration for the latent-space experiments. All methods are trained from scratch, except for MeanFlow [13] where we use the pretrained checkpoint from a popular PyTorch reproduction [57] as our baseline. Training is partial in all latent-space experiments. On ImageNet, we train for 80 epochs, matching the ablation budget in Tab. 1 of the original paper [13]. On FFHQ, we use a comparable number of training steps. For the classifier-free guidance (CFG) setting, the same iteration count is reached with a larger batch size for efficiency, and we use a guidance scale of 1.5 at inference following prior work [38].

Prior construction. In all experiments, we set $\alpha = 0.5$ (Eq. (5)) for training v_θ . The low-frequency prior is obtained by downsampling by a factor of 4 in each spatial dimension, applied to pixels for CIFAR-10 and to latents for FFHQ and ImageNet. Alg. A.1 provides a PyTorch-style pseudocode implementation of the training and inference procedures.

Inference overhead. Our two-stage pipeline introduces a small fixed overhead from the lightweight generator G_ϕ , which operates on 8×8 representations using a smaller variant of the main architecture (for SiT models, SiT-S/2 with 16 tokens, compared to SiT-B/4 with 64 tokens for v_θ). Fig. A.1 reports the wall-clock time per step for both models across batch sizes. One G_ϕ step consistently takes $\approx 0.08\text{--}0.09\times$ the time of a v_θ step, so the 8 generation steps used for G_ϕ amount to ≈ 0.72 effective NFE of overhead. This cost is fixed regardless of the number of main-model steps, meaning the relative overhead shrinks as NFE increases.

A.2 Compute resources

Experiments were run on a heterogeneous mix of NVIDIA A5000, A6000, and H100 GPUs. For a uniform reporting unit, we report the wall-clock training time of a single run on one A5000-equivalent

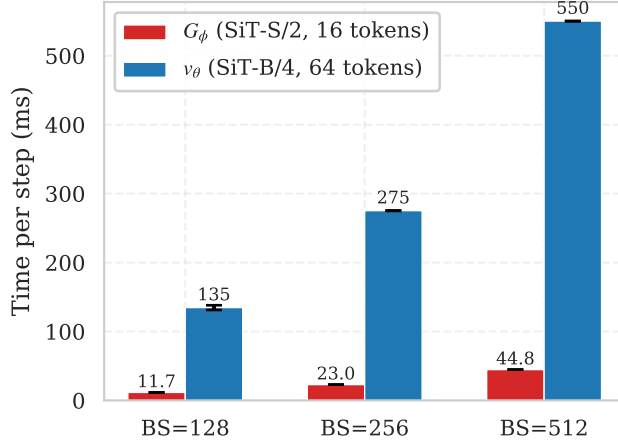


Figure A.1: v_θ vs. G_ϕ **Wall Time**. Inference time per step (ms) for the low-frequency generator G_ϕ (SiT-S/2, 16 tokens) and the main model v_θ (SiT-B/4, 64 tokens) across different batch sizes. One G_ϕ step is ≈ 0.08 – 0.09 steps of v_θ .

GPU (training only, excluding evaluation), separately for the main flow model v_θ and the lightweight low-frequency generator G_ϕ : CIFAR-10: $v_\theta \approx 28$ h, $G_\phi \approx 1.5$ h; FFHQ-256: $v_\theta \approx 25$ h, $G_\phi \approx 2.5$ h; MeanFlow ImageNet-256: $v_\theta \approx 260$ h, $G_\phi \approx 24$ h. G_ϕ thus adds ~ 5 – 10% on top of the main-model training cost.

A.3 Curvature

To quantify trajectory straightness, we report the curvature metric used in prior work [36, 34], which measures the deviation of the learned trajectory from a straight path,

$$C = \mathbb{E}_t \left[\|(x_1 - x_0) - v_\theta(x_t, t)\|^2 \right], \quad (\text{A.1})$$

where $v_\theta(x_t, t)$ is the learned velocity and $x_1 - x_0$ is the constant velocity of the straight-line path. A perfectly straight trajectory has zero curvature. Following Lee *et al.* [34], we evaluate on 10,000 generated samples using 128 Euler steps.

A.4 Inference-time noise calibration

At inference, the starting point is constructed from $\mathcal{U}(\hat{x}_1^\downarrow)$ by adding Gaussian noise at level α (Fig. 2c), according to Eq. (5). During training, this is set to $\alpha = 0.5$. At inference, we find that a slightly higher noise level $\alpha^* = \alpha + \varepsilon$, with $\varepsilon > 0$, consistently improves FID, particularly in the few-step regime. This is consistent with observations in score-based generative modeling [49], where slightly expanding the support of a concentrated distribution improves the conditioning of the learned vector field and reduces artifacts at inference time.

Across all benchmarks, the optimal inference noise follows $\alpha^* = \alpha_{\text{train}} + \varepsilon$, where $\varepsilon > 0$ is a small excess that decreases with the number of function evaluations. In the few-step regime (up to 4 effective NFE), we find $\varepsilon \approx 0.05$ in both pixel space (CIFAR-10) and latent space (FFHQ, ImageNet), consistent across datasets and resolutions. For MeanFlow, the effect is milder ($\varepsilon \approx 0.01$), consistent with its single-step formulation being less sensitive to the source distribution.

B Empirical validation

B.1 OT preservation under noise

This section provides extended details for the experiment in Fig. 3, including the FID-vs- α and pairwise-distance plots.

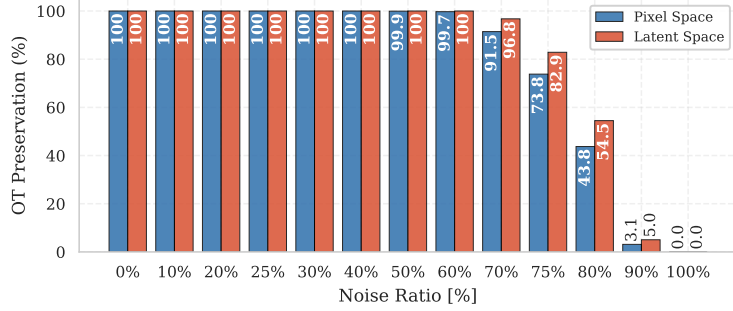


Figure B.2: **Comparison of noise ratio vs. OT preservation.** An elaborated version of Fig. 3 showing the OT preservation metric as a function of the noise ratio α in Eq. (5).

OT coupling preservation. In Fig. 3, we measure the fraction of training pairs for which the exact discrete OT assignment (computed using the POT library) coincides with the identity coupling, as the noise level α in Eq. (5) increases. The experiment uses 10,000 CIFAR-10 samples in pixel space and 10,000 FFHQ samples in the latent representation of a pretrained autoencoder [44, 38]. Fig. B.2 extends this analysis to finer noise-ratio increments, confirming that the identity coupling is fully preserved up to $\alpha \approx 0.5$.

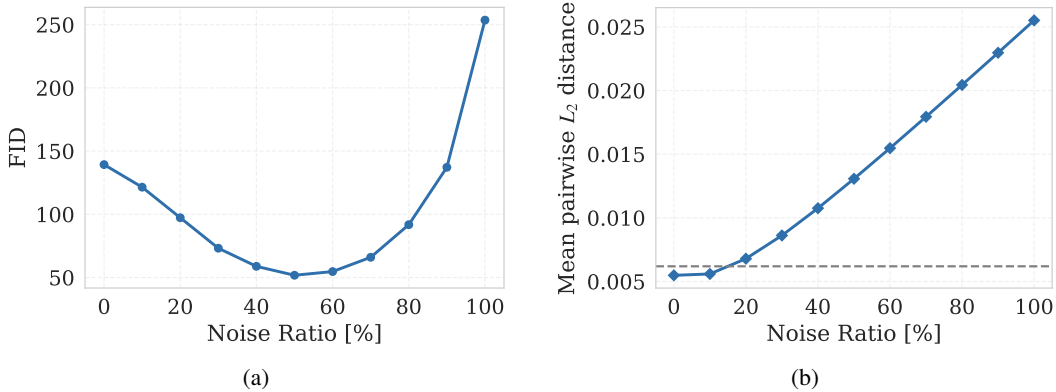


Figure B.3: **Effect of noise ratio α on generation quality and prior spread.** (a) FID on CIFAR-10 (2 NFE) vs. noise ratio. (b) Pairwise ℓ_2 distance on CIFAR-10 vs. noise ratio; *dashed*: original images.

FID vs. noise ratio. Fig. B.3a reports FID on CIFAR-10 as a function of α , evaluated at 2 NFE after an early training stage of 40,000 steps (10% of full training). Quality improves from $\alpha = 0$ to $\alpha = 0.5$, then degrades as noise overwhelms the low-frequency structure.

Pairwise distance analysis. Fig. B.3b (discussed in Sec. 4.1) shows the mean pairwise ℓ_2 distance between prior samples as a function of α (proportional to noise ratio). At $\alpha = 0$, the mean pairwise distance between low-frequency projections on CIFAR-10 is $\approx 5.4 \times 10^{-3}$ (normalized by $d = 3,072$), roughly 11% below the original-image distance of $\approx 6.1 \times 10^{-3}$. This concentration is consistent with the $1/f^2$ spectral decay of natural images [11], which places the majority of image energy in the lowest frequencies. As α increases, the noise term dominates and the mean pairwise distance grows steadily.

In the main text (Eq. (6)), we state that the cross term vanishes and the expected distance decomposes into a projection term and a noise term. We now show this step by step. Expanding the squared distance between two noisy prior samples $x_0^{(i)}$ and $x_0^{(j)}$ constructed via Eq. (5). Expanding the squared norm,

$$\|x_0^{(i)} - x_0^{(j)}\|^2 = \|(1 - \alpha)(T(x^{(i)}) - T(x^{(j)})) + \alpha(\epsilon^{(i)} - \epsilon^{(j)})\|^2. \quad (\text{B.2})$$

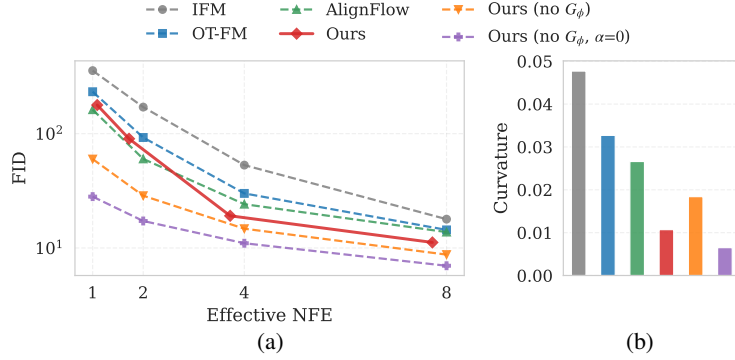


Figure B.4: **Oracle Experiment on CIFAR-10.** FID (\downarrow) vs. effective NFE and trajectory curvature (\downarrow) for baselines, our full pipeline, and two oracle conditions that bypass G_ϕ using true training-image projections. Panels (a) and (b) show FID and curvature, respectively. *Ours (no G_ϕ)*: $\alpha = 0.5$. *Ours (no G_ϕ , $\alpha=0$)*: deterministic coupling.

Since the noise terms are independent of the data and of each other, the cross term vanishes in expectation,

$$\mathbb{E}[\|x_0^{(i)} - x_0^{(j)}\|^2] = (1 - \alpha)^2 \mathbb{E}[\|T(x^{(i)}) - T(x^{(j)})\|^2] + 2\alpha^2 d, \quad (\text{B.3})$$

where d is the data dimensionality and the last term follows from $\epsilon^{(i)} - \epsilon^{(j)} \sim \mathcal{N}(0, 2I_d)$. The first term captures the pairwise spread in the projected subspace, scaled down by $(1 - \alpha)^2$, while the second grows linearly with d , explaining the steady increase visible in Fig. B.3b.

B.2 Oracle experiment

To isolate the effect of G_ϕ on generation quality, we evaluate two oracle conditions alongside our full pipeline on CIFAR-10. Both bypass G_ϕ entirely, constructing starting points directly from training images.

Oracle conditions. *Oracle prior* uses our standard training procedure ($\alpha = 0.5$) but replaces G_ϕ at inference with exact prior samples as in Eq. (5) derived from training images. *Deterministic oracle* trains with $\alpha = 0$ (fully deterministic coupling, $x_0 = T(x_1)$) and starts inference from the exact projections $T(x_i)$. Fig. B.4 reports FID and curvature for all conditions.

Results. Both oracle conditions achieve lower FID than the full pipeline across all step counts, confirming that improving G_ϕ can further close the gap to oracle-level performance. The deterministic oracle achieves the best FID and the lowest curvature overall, consistent with the theoretical optimality of the projection-based coupling.

An interesting exception is that the full pipeline with G_ϕ achieves *lower* curvature than the noised oracle, despite worse FID. We hypothesize that this is because the noised oracle starts near specific training projections, so when two projections $T(x_i)$ and $T(x_j)$ are close, the velocity field must reconcile conflicting transport directions within a small neighborhood, increasing curvature. G_ϕ , by contrast, produces samples that land between training projections rather than near any specific one, in regions where the velocity field may be smoother and more internally consistent.

C Ablation studies

C.1 Projection variants

This section accompanies the claim in Sec. 4.1 that OT-optimality of the identity coupling is necessary but not sufficient for our prior design. We compare four candidate transformations T , each an orthogonal projection that retains 1/16 of the input dimensionality. For all four, the identity coupling $x_i \mapsto T(x_i)$ is OT-optimal by construction (Props. D.1 and D.2), yet only the low-frequency members yield a usable prior in practice.

Table C.3: **Projection Variants on CIFAR-10.** Four projections (strictly orthogonal except for bicubic downsampling), each retaining 1/16 of the input dimensionality, trained for 150,000 steps under Eq. (5) at $\alpha = 0$ and $\alpha = 0.5$. FID and curvature are evaluated at 1 NFE in the oracle condition (real test images projected through T , G_ϕ bypassed). Reconstruction MSE is $\mathbb{E} \|T(x) - x\|^2$ on the training set. Hungarian assignment confirms 100% OT-identity preservation for every operator at both noise levels. The shaded row is the operator used throughout the paper. Best per column in bold.

Operator	MSE (\downarrow)	$\alpha = 0$		$\alpha = 0.5$	
		FID (\downarrow)	Curv. (\downarrow)	FID (\downarrow)	Curv. (\downarrow)
Bicubic	0.009	102.05	5.0×10^{-6}	87.82	0.013
Fourier truncation	0.010	119.29	1.2×10^{-5}	87.99	0.013
Random pixel mask	0.271	117.90	1.5×10^{-3}	226.72	0.022
Random patch mask	0.271	144.95	1.4×10^{-3}	205.57	0.023

Operator family. We instantiate four orthogonal projections on CIFAR-10 images ($32 \times 32 \times 3$). *Bicubic* sets $T = \mathcal{U} \circ \mathcal{D}$ with \mathcal{D} area downsampling $32 \times 32 \rightarrow 8 \times 8$ and \mathcal{U} bicubic upsampling (the operator used throughout the paper). *Fourier truncation* keeps the lowest-frequency 8×8 block of DFT coefficients per channel and zeros the rest. *Random pixel mask* applies a fixed binary mask, sampled once and held constant across all images, that retains a random subset of 1/16 of the pixels. *Random patch mask* applies a fixed binary mask over an 8×8 grid of 2×2 patches, retaining 1/16 of the patches. A diagonal 0/1 mask is symmetric and idempotent, so both masking operators are valid orthogonal projections. The first two preserve low-frequency structure. The last two do not.

Setup. For each operator we train v_θ at the full CIFAR-10 capacity (Tab. A.1) for 150,000 steps under the noisy prior of Eq. (5), once at $\alpha = 0$ and once at $\alpha = 0.5$. We evaluate in the oracle condition of Sec. B.2, i.e., starting points are drawn from real test images projected through T rather than from the prior generator G_ϕ . This isolates the effect of the projection operator on v_θ from the quality of the lightweight prior model. Reconstruction MSE $\mathbb{E} \|T(x) - x\|^2$ on the training set is the squared transport cost paid by the identity coupling under the OT objective of Eq. (4). We additionally verify OT-identity preservation empirically by computing the exact discrete OT assignment on 10,000 pairs (Hungarian algorithm) for each operator at both noise levels. Preservation is 100% in all eight settings, confirming that all four operators are OT-equivalent under our objective, both deterministically and under the $\alpha = 0.5$ noise interpolation.

Results. Tab. C.3 confirms the necessary-but-not-sufficient claim. Reconstruction MSE splits the operators into two groups, with the low-frequency family (0.009 and 0.010) roughly $30\times$ lower than the masking family (0.271 for both). This reflects the spectral structure of natural images, under which the lowest 8×8 frequency block captures most of the ℓ_2 energy, while 1/16 of the pixels or 1/16 of 2×2 patches do not.

At $\alpha = 0$, the low-frequency operators yield curvature in the 10^{-6} to 10^{-5} range, while the masking operators sit two to three orders of magnitude higher ($\sim 1.4 \times 10^{-3}$). FID at $\alpha = 0$ is dominated by the masking operators’ high reconstruction error, so v_θ is asked to in-paint 15/16 of the pixels from a starting point that is largely zeros, which is closer to the original generation problem than to a residual-detail problem.

At $\alpha = 0.5$, the regime we adopt, the gap widens. Bicubic and Fourier truncation recover FID ≈ 88 , while the masking operators degrade to FID above 200. Two effects combine. The transport cost paid by the masking operators, though OT-optimal among permutations, is intrinsically high because the projection itself discards most of the signal. And the prior support of the masking operators is concentrated on pixel-level discontinuities that are not stable under additive Gaussian noise, so v_θ must traverse a fragmented prior on its way to the data manifold.

OT-optimality is therefore necessary but not sufficient. Hungarian preservation is 100% for every operator and every noise level we test, so the discriminating factor between operators is not the OT property but the tractability of the induced prior. Within the low-frequency family, bicubic edges out Fourier truncation on reconstruction MSE, matches it at $\alpha = 0.5$, and is the operator we adopt.

C.2 Downsampling factor

The downsampling factor controls the dimensionality of the low-frequency prior and directly affects the trade-off between prior informativeness and tractability. Too little downsampling retains high-frequency content, leaving G_ϕ with a generation task comparable in difficulty to the original problem and negating the benefit of a lightweight first stage. Too much downsampling discards structure needed for the flow model to produce high-quality samples. Fig. C.5 compares $4\times$ and $8\times$ spatial downsampling on CIFAR-10. A $4\times$ reduction (8×8 prior from 32×32 images) yields consistently better FID across step counts, while $8\times$ downsampling degrades quality as the prior loses too much structural detail to serve as an effective starting point. We adopt $4\times$ in all experiments.

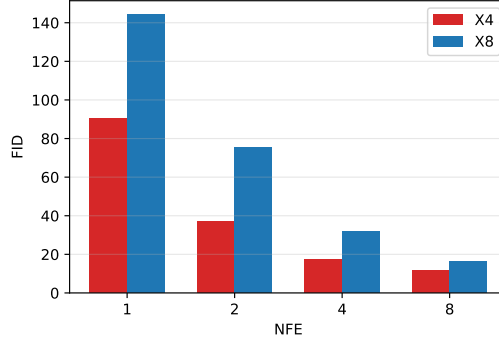


Figure C.5: **Downsample factor ablation on CIFAR-10.** FID as a function of NFE for two spatial downsampling factors ($\times 4$) and ($\times 8$). A lower downsampling factor consistently yields better FID across all NFE budgets

C.3 G_ϕ step count

The number of ODE steps used by G_ϕ determines both the quality of the low-frequency prior and the generation-time overhead. Since our method targets the few-step regime, we select the number of G_ϕ steps to keep the prior-generation overhead below 1 effective NFE, ensuring fair comparison against single-step and two-step baselines.

Fig. C.6 reports FID as a function of effective NFE on CIFAR-10, sweeping G_ϕ steps over $\{1, 2, 4, 8, 16\}$ and v_θ steps over $\{1, 2, 4, 8\}$. At 1 v_θ step, using 16 G_ϕ steps yields better FID than 8 steps, but at a higher effective NFE (≈ 2.4 vs. 1.7). As the v_θ step count increases, the advantage of additional G_ϕ steps diminishes. At $2+ v_\theta$ steps, 8 G_ϕ steps achieve comparable or better FID than 16 at lower effective NFE. We therefore use 8 steps for G_ϕ in all experiments, yielding an overhead of ≈ 0.72 effective NFE (see the Inference Overhead paragraph in Sec. A.1). Notably, even a single G_ϕ step produces competitive results, confirming that the low-frequency distribution is sufficiently smooth for coarse approximation at minimal cost.

D Proofs and formal details

Proposition D.1 (Orthogonal projections preserve self-proximity). *Let $T: \mathbb{R}^d \rightarrow \mathbb{R}^d$ be an orthogonal projection, i.e., $T^2 = T$ (idempotent) and $T^\top = T$ (symmetric). Then for any $x, x' \in \mathbb{R}^d$,*

$$\|T(x') - x\|^2 = \|T(x) - x\|^2 + \|T(x') - T(x)\|^2. \quad (\text{D.4})$$

In particular, $\|T(x) - x\| \leq \|T(x') - x\|$, with equality iff $T(x') = T(x)$.

Proof. Denote $\delta = x' - x$. By linearity of T ,

$$T(x') - x = T(x) + T(\delta) - x = T(\delta) + (T(x) - x). \quad (\text{D.5})$$

The first term $T(\delta) \in \text{Im}(T)$. For the second, note that by idempency

$$T(T(x) - x) = T^2(x) - T(x) = 0. \quad (\text{D.6})$$

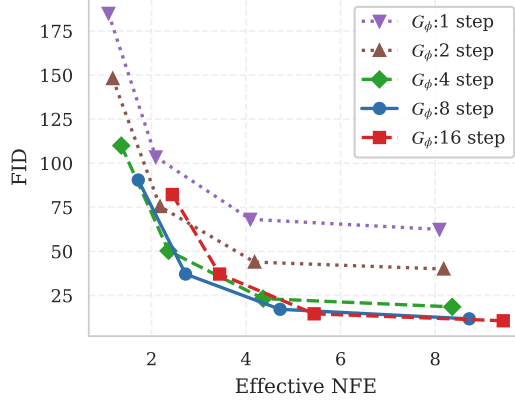


Figure C.6: G_ϕ Step Count Ablation on CIFAR-10. Each curve fixes the number of G_ϕ steps (legend) and sweeps v_θ over $\{1, 2, 4, 8\}$ steps. The x-axis reports effective NFE, the total generation cost combining both G_ϕ and v_θ steps (G_ϕ steps weighted at $0.09\times$). At 1 v_θ step, 16 G_ϕ steps improve FID over 8 at higher effective NFE. From 2 v_θ steps onward, 8 G_ϕ steps achieve similar FID to 16 at lower effective cost.

so $(T(x) - x) \in \ker(T)$. For an orthogonal projection, $\text{Im}(T)$ and $\ker(T)$ are orthogonal subspaces, so by the Pythagorean theorem,

$$\|T(x') - x\|^2 = \|T(\delta)\|^2 + \|Tx - x\|^2 = \|T(x') - T(x)\|^2 + \|T(x) - x\|^2. \quad (\text{D.7})$$

□

□

Proposition D.2 (Discrete OT optimality of projections). *Let $P: \mathbb{R}^d \rightarrow \mathbb{R}^d$ be an orthogonal projection, and let $\{x_1, \dots, x_n\} \subset \mathbb{R}^d$ be a finite point set with distinct projections, i.e., $Px_i \neq Px_j$ for $i \neq j$. Then the identity assignment $\sigma = \text{id}$, mapping $x_i \mapsto Px_i$, minimizes the total transport cost*

$$C(\sigma) = \sum_{i=1}^n \|Px_{\sigma(i)} - x_i\|^2 \quad (\text{D.8})$$

over all permutations σ of $\{1, \dots, n\}$.

Proof. By Prop. D.1, for any i and any $j \neq i$,

$$\|Px_j - x_i\|^2 = \|Px_i - x_i\|^2 + \|Px_j - Px_i\|^2.$$

Since the projections are distinct, $\|Px_j - Px_i\|^2 > 0$, so

$$\|Px_i - x_i\|^2 < \|Px_j - x_i\|^2. \quad (\text{D.9})$$

Every point x_i is therefore strictly closer to its own projection than to the projection of any other point.

Now consider any permutation $\sigma \neq \text{id}$. There exists at least one index i with $\sigma(i) \neq i$. For that index, $\|Px_{\sigma(i)} - x_i\|^2 > \|Px_i - x_i\|^2$. Since $\|Px_{\sigma(j)} - x_j\|^2 \geq \|Px_j - x_j\|^2$ for all j , with strict inequality for at least one, we have $C(\sigma) > C(\text{id})$. □

Remark (Low-pass filtering as orthogonal projection). *The discrete Fourier transform (DFT) is a unitary transformation. Let F denote the DFT matrix and let P_S be the diagonal matrix that retains a subset S of Fourier coefficients and zeros out the rest. P_S is an orthogonal projection in the frequency domain. Since conjugation by a unitary preserves orthogonal projections, $P = F^{-1}P_SF$ is an orthogonal projection in pixel space. In particular, choosing S to be the lowest-frequency coefficients yields low-pass filtering, so Props. D.1 and D.2 apply directly.*

In our pipeline (Sec. 4.2), the transformation $T = \mathcal{U} \circ \mathcal{D}$ applies downsampling \mathcal{D} followed by upsampling \mathcal{U} . When both operations use nearest-neighbor interpolation, T is exactly an orthogonal projection onto the subspace of block-constant images, and the OT guarantee holds by construction. In practice, we find it better to use area interpolation for \mathcal{D} and bicubic interpolation for \mathcal{U} , which is not strictly orthogonal but yields lower reconstruction error, and the OT structure is preserved empirically as confirmed in Fig. 3.

E Qualitative results

We visualize how the noise level α in Eq. (5) affects the structure of the prior x_0 , in pixel space (CIFAR-10, Sec. E.1) and latent space (FFHQ, Sec. E.2). As α increases, the low-frequency content that underlies the OT coupling is progressively obscured, consistent with the quantitative analysis in Fig. 3 and Sec. B.1.

E.1 Pixel-space prior (CIFAR-10)

Fig. E.7 shows representative CIFAR-10 samples across all noise levels. Each column displays the original image x_1 , its low-frequency projection $T(x_1)$, and the noised starting point x_0 for $\alpha \in \{0, 0.1, \dots, 1\}$. At low noise levels, the dominant color, spatial layout, and coarse object structure of the original image remain clearly visible, consistent with the quantitative OT preservation reported in Fig. 3. Around $\alpha \approx 0.5$, noise begins to dominate and the visual correspondence to the original gradually fades.

E.2 Latent-space prior (FFHQ)

Fig. E.8 shows the same visualization for FFHQ in the latent space of a pretrained autoencoder [44]. Each column displays the original image, its encoded latent, the downsampled latent $x_1^\downarrow = \mathcal{D}(x_1)$, and x_0 at increasing α values. Unlike pixel space, the structural correspondence is harder to assess visually in latent representations, particularly at moderate noise levels. This is precisely why the quantitative validation in Fig. 3 is important, where the identity coupling is preserved at 100% up to $\alpha = 0.5$ even in latent space.

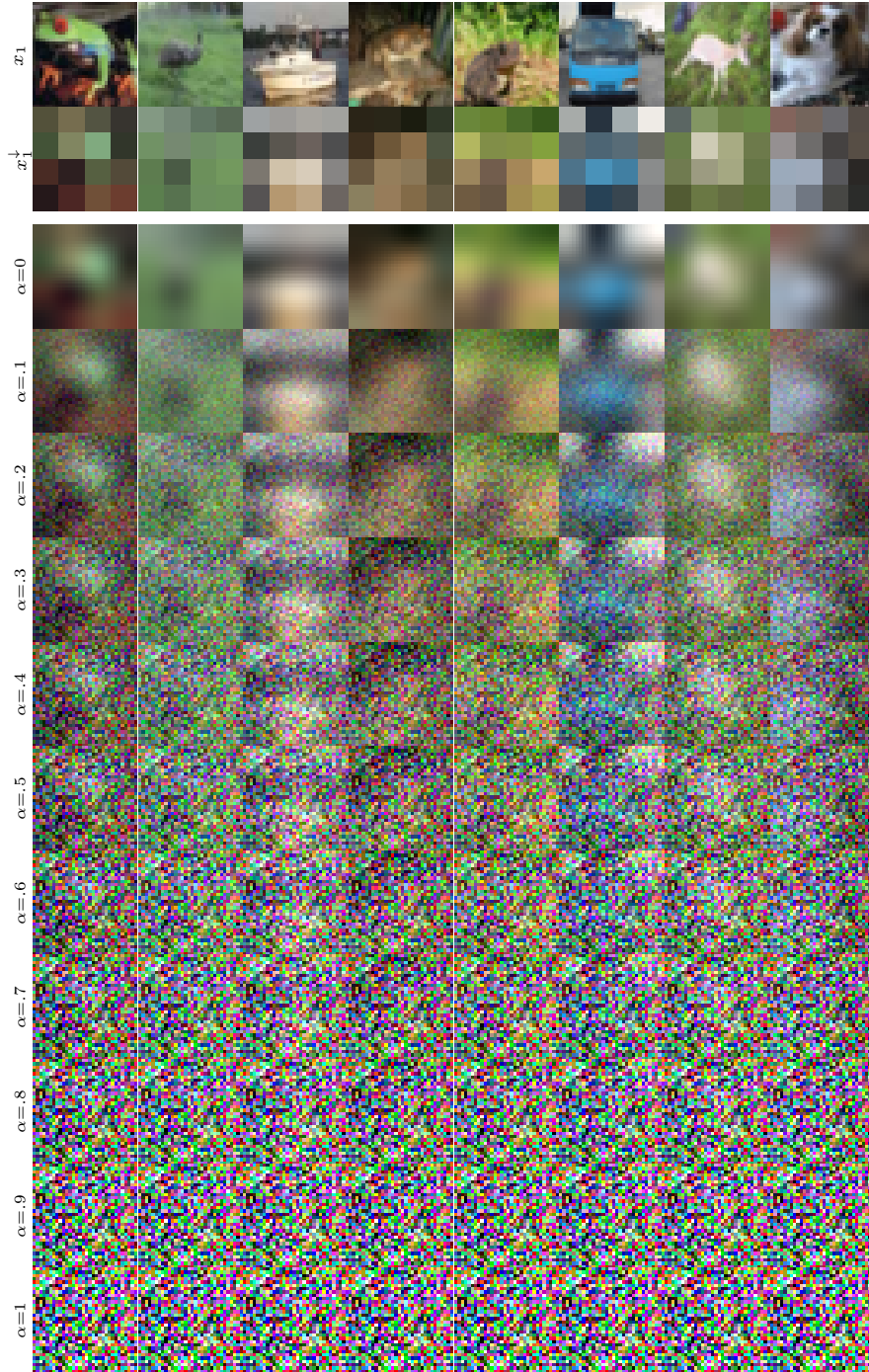


Figure E.7: **Prior Construction on CIFAR-10.** Each column shows one training image x_1 (top), its low-frequency representation $x_1^\downarrow = \mathcal{D}(x_1)$, and the noised starting point $x_0 = (1 - \alpha)\mathcal{U}(x_1^\downarrow) + \alpha \epsilon$ (Eq. (5)) at increasing noise levels, ranging from the pure upsampled projection ($\alpha=0$) through the operating point ($\alpha=0.5$), where coarse structure remains visible, to pure Gaussian noise ($\alpha=1$).

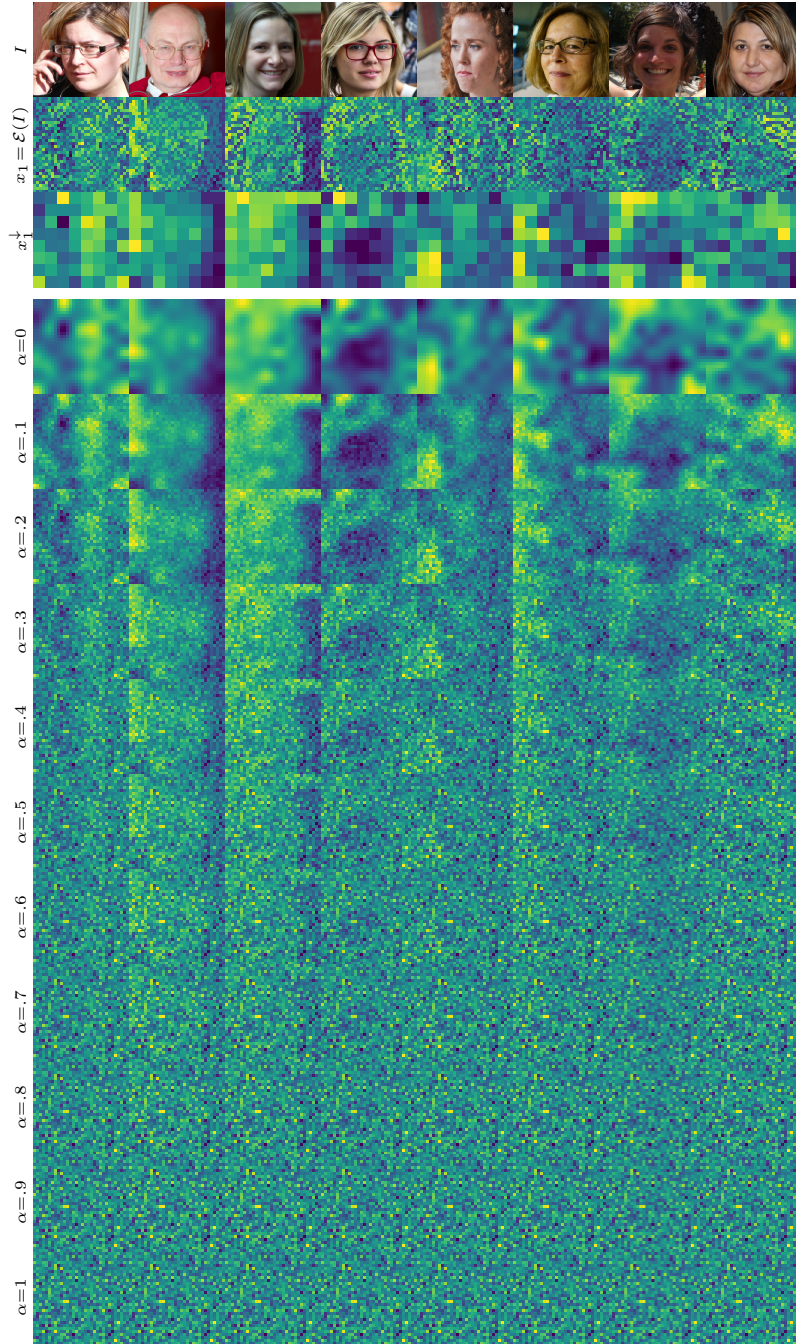


Figure E.8: **Prior Construction on FFHQ (Latent Space)**. The first row shows original images x_1 for reference. The second row visualizes the corresponding latent encoding, and the third row its low-frequency representation $x_1^\downarrow = \mathcal{D}(x_1)$. Subsequent rows show the noised starting point $x_0 = (1 - \alpha)\mathcal{U}(x_1^\downarrow) + \alpha\epsilon$ (Eq. (5)) at increasing noise levels, ranging from the pure upsampled projection ($\alpha=0$) through the operating point ($\alpha=0.5$) to pure noise ($\alpha=1$). All operations from the third row onward are applied in the latent space of a pretrained autoencoder [44].